Oxidation of Metals (2020) 94:431–445
https://doi.org/10.1007/s11085-020-10000-z

ORIGINAL PAPER

Microscopic Investigation of High-Temperature Oxidation of hcp-$ZrAl_2$

Zhangping Hu[1] · Yifei Xu[1] · Zongqing Ma[1] · Chong Li[1] · Yuan Huang[1] · Yongchang Liu[1] · Zumin Wang[1]

Received: 29 November 2019 / Revised: 5 August 2020 / Published online: 4 September 2020

Abstract

The high-temperature oxidation of $ZrAl_2$ upon exposure to pure O_2 at 800–950 °C was studied in terms of the oxidation kinetics and the formation mechanism of the oxide layer. The alloy followed parabolic oxidation kinetics, and the activation energy of oxidation was 239 ± 14 kJ/mol. During the early stages of oxidation below 850 °C, a single-layer oxide formed due to the crystallization of the initially formed amorphous oxide layer. A multilayer oxide structure developed at higher temperatures, due to the slightly higher affinity of oxygen for Zr than for Al and the oxidation-induced compositional changes.

Keywords Thermal oxidation · Zr–Al alloys · Multilayer oxide · Oxidation kinetics

Introduction

The surficial oxide layers are inevitably formed on the in-service functional and structural materials, which intensively determines their surface-related properties, such as corrosion resistance, catalytic activity, friction, wear and long-term reliability [1–4]. The compositions and microstructures of the oxide layers are governed by many factors, such as oxidation conditions (including temperature, time and oxygen partial pressure [5]), atomic structure and composition of the parent alloys [6].

Zr-M (M = Al, Sn, Mo and Nb) binary alloys possess good physical properties, such as good high-temperature creep resistances and low thermal expansion coefficients [7–13], and thus are widely used as fuel cladding materials for pressurized-water reactor [14, 15] and hydrogen absorbing agents [16]. Among the Zr–M binary alloy family, Zr–Al alloys attract intensive attentions due to their excellent

✉ Chong Li
lichongme@tju.edu.cn

✉ Zumin Wang
z.wang@tju.edu.cn

[1] School of Materials Science and Engineering, Tianjin University, Tianjin 300350, China

physical properties, such as high thermal conductivity, high hardness and superelastic properties [17–22]. $ZrAl_2$ alloy has the highest bulk modulus, shear modulus and Young's modulus among the various Zr–Al intermetallic phases [23, 24], as shown in the phase diagram of Zr–Al binary system (Fig. 1) [25]. The atomic structure of $ZrAl_2$ is similar to the topologically close-packed (TCP) $MgZn_2$ (Laves phase) [26], which can result in a good high-temperature stability. Therefore, $ZrAl_2$ is a promising high-temperature structural material, for example, in thermonuclear reactors [26, 27].

The thermal oxidation of $ZrAl_2$ alloys in the temperature range of 350–750 °C has been studied [6, 28]. Synchronous oxidation of Zr and Al in the $ZrAl_2$ alloy results in the formation of amorphous $(Zr_{0.33}Al_{0.67})O_{1.66}$ oxide layers with a thickness of tens of nanometers to several micrometers. The amorphous Zr–Al–O oxide with a stoichiometric composition of $(Zr_{0.33}Al_{0.67})O_{1.66}$ is thermodynamically stable with a lowest Gibbs forming energy in the Al_2O_3–ZrO_2 binary system [5], and can stay amorphous at the temperature up to 750 °C [28]. However, the structural material in e.g., thermonuclear reactors often serves at higher temperatures up to 1000 °C. To this end, a systematic oxidation study of $ZrAl_2$ alloy at temperatures higher than 750 °C is urgently needed. The small difference between the affinities of Zr and Al toward oxygen [6] can have a strong influence on the oxidation behaviors at higher temperatures, which may disrupt the formation of the thermally stable amorphous Zr–Al–O oxide overlayer.

In this paper, the thermal oxidation of $ZrAl_2$ alloy at the temperature range of 800–950 °C is investigated by a combinational experimental approach including optical microscopy (OM), X-ray diffraction (XRD), cross-sectional scanning electron microscopy (SEM), and thermogravimetric analysis (TGA). The role of

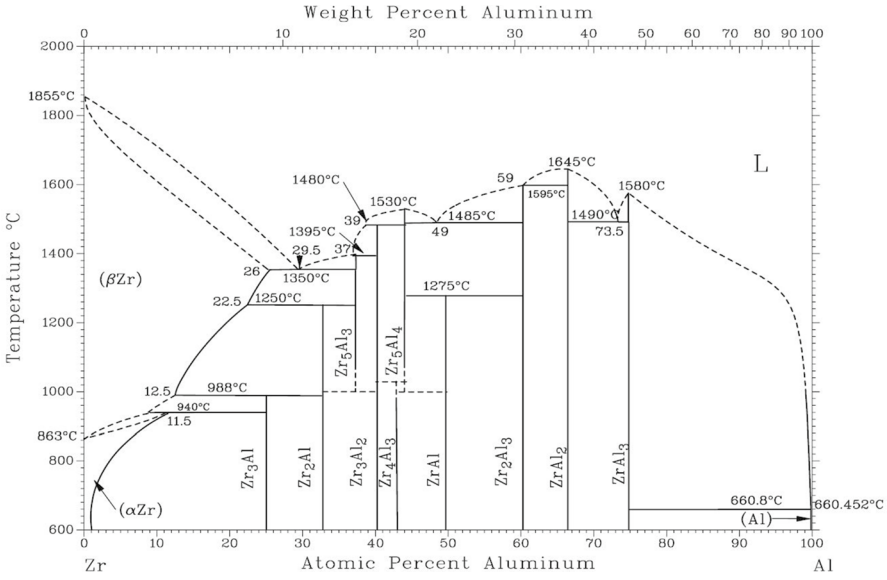

Fig. 1 Zr–Al alloy phase diagram [25]

small differences in the oxygen affinities of alloy constituents at high oxidation temperatures on the oxidation behaviors is revealed.

Experimental Procedures

Specimen Preparation and Thermal Oxidation

The $ZrAl_2$ alloy ingots were prepared by magnetic levitation melting technology. Further details of this procedure can be found elsewhere [28]. The as-cast $ZrAl_2$ was confirmed by XRD to be single phase with a hexagonal close-packed (hcp) structure ("Microstructural and Compositional Characterizations" section). Specimens with dimensions of 6 mm × 5 mm × 3 mm were cut from the $ZrAl_2$ alloy ingots by wire electro-discharge machining. All six surfaces of each specimen were polished by using polishing papers and diamond polishing liquid, ultrasonically cleaned, and dried by a stream of compressed N_2. Finally, the initial mass of each $ZrAl_2$ specimen was measured by an electronic balance (Sartorius Bsa 124S) with a resolution of 0.1 mg.

Each experiment of isothermal oxidation was done separately. The isothermal experiment process is as follows. The as-polished $ZrAl_2$ specimen was inserted into a separate quartz tube (inner diameter: 17 mm, outer diameter: 20 mm and length: 250 mm). The tube was evacuated, backfilled with pure oxygen (purity ≥ 99.999 vol%), and sealed using a rotary vacuum sealing device (MRVS-3002, Partulab Technology). To ensure an oxygen partial pressure of $pO_2 = 1 \times 10^5$ Pa at the oxidation temperatures of 800 °C, the oxygen partial pressure was set to 2.8×10^4 at room temperature (RT) in the tube. The $ZrAl_2$ specimen in the quartz tube was then subjected to isothermal oxidation for 3 h in a tube furnace (OTF-1200X) preheated at 800 °C. The oxidized specimen was removed from the furnace and cooled naturally to RT. The above steps were repeated with fresh $ZrAl_2$ specimens for other isothermal oxidation experiments for 6, 12, 18 and 24 h at 800 °C. Similarly, the isothermal oxidation experiments were also carried out at 850 °C ($pO_2 = 2.7 \times 10^4$ Pa at RT), 900 °C ($pO_2 = 2.5 \times 10^4$ Pa at RT) and 950 °C ($pO_2 = 2.4 \times 10^4$ Pa at RT) for different oxidation times (3, 6, 12, 18 and 24 h), respectively. The masses of the $ZrAl_2$ specimens oxidized at different oxidation temperatures for different times were measured using an electronic balance to calculate the mass gain after thermal oxidation. For all experiments, no scale spalling could be observed by optical microscope.

X-ray Diffraction and Microstructural Characterization

The phase constitution of the oxidized $ZrAl_2$ specimens was investigated by XRD. To this end, the XRD diffractograms of the specimens before and after oxidation were recorded over a diffraction angle 2θ range of 20°–70° with a step size of 0.2° using a Bruker D8 Advance diffractometer with a Cu-Kα radiation anode (40 kV/40 mA, $\lambda = 1.5418$ Å).

The metallographic structure of the as-cast $ZrAl_2$ was investigated by optical microscopy (OM, OLYMPUS GX51F). The cross-sectional microstructure of the as-oxidized $ZrAl_2$ was investigated by SEM in backscattered electron (BSE) mode (JEOL JSM-7800F) equipped with an energy-dispersive x-ray spectrometer (EDX, EDAX Octane Plus). The spatial distributions of elements in the $ZrAl_2$ specimens oxidized at different oxidation temperatures for different oxidation times were investigated by EDX line scans and EDX mapping along the cross sections of the specimens.

Results

Microstructural and Compositional Characterizations

The original metallographic structure of the as-cast $ZrAl_2$ observed by optical microscopy is shown in Fig. 2a. The grain sizes of the as-cast $ZrAl_2$ varied over a range of 10–100 μm. Therefore, the grain-boundary (GB) density in the as-cast $ZrAl_2$ was rather low, and the effect of the GBs on the oxidation process in the investigated $ZrAl_2$ can be neglected. The XRD pattern shown in Fig. 2b confirms that the as-cast $ZrAl_2$ specimens possessed a hexagonal close-packed (hcp) structure. After thermal oxidation, the observation of a broad diffraction hump suggested that an

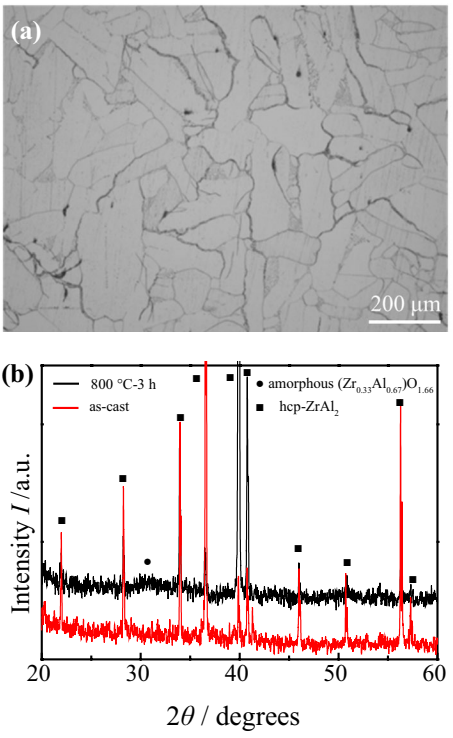

Fig. 2 **a** The OM image of the as-cast $ZrAl_2$, **b** XRD pattern of the as-cast $ZrAl_2$ alloy and the $ZrAl_2$ alloy oxidized at 800 °C for 3 h

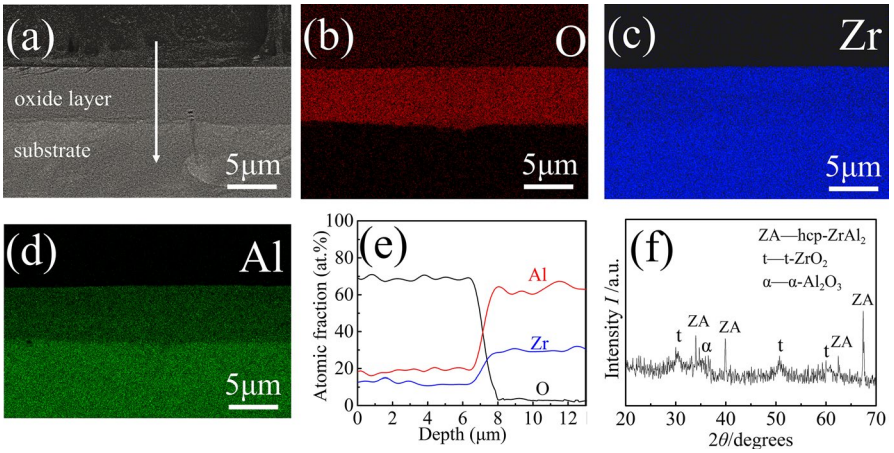

Fig. 3 **a** Cross-sectional BSE micrographs, image of **b** O, **c** Zr and **d** Al EDX mappings, **e** cross-sectional EDX line profile, and **f** XRD patterns of $ZrAl_2$ oxidized at 800 °C for 12 h. The white arrows in the figures indicate the scan direction of the EDX line

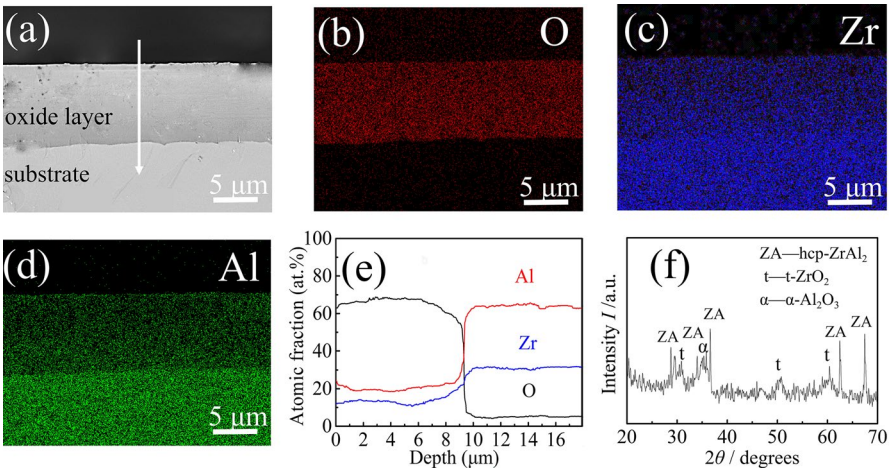

Fig. 4 **a** Cross-sectional BSE micrographs, image of **b** O, **c** Zr and **d** Al EDX mappings, **e** cross-sectional EDX line profile, and **f** XRD patterns of $ZrAl_2$ oxidized at 800 °C for 24 h. The white arrows in the figures indicate the scan direction of the EDX line

amorphous oxide formed on the $ZrAl_2$ surface at 800 °C for 3 h (Fig. 2b). According to a recent study of $ZrAl_2$ oxidized in the 550–750 °C range, the composition of the amorphous oxide layer was $(Zr_{0.33}Al_{0.67})O_{1.66}$ [28].

The evolution of the composition and microstructure of the surface oxide layer during the oxidation process was further investigated by XRD, cross-sectional BSE, cross-sectional EDX mapping, and line scanning. The XRD patterns of the $ZrAl_2$ oxidized at different temperatures for different times are shown in Figs. 3, 4, 5, 6, 7,

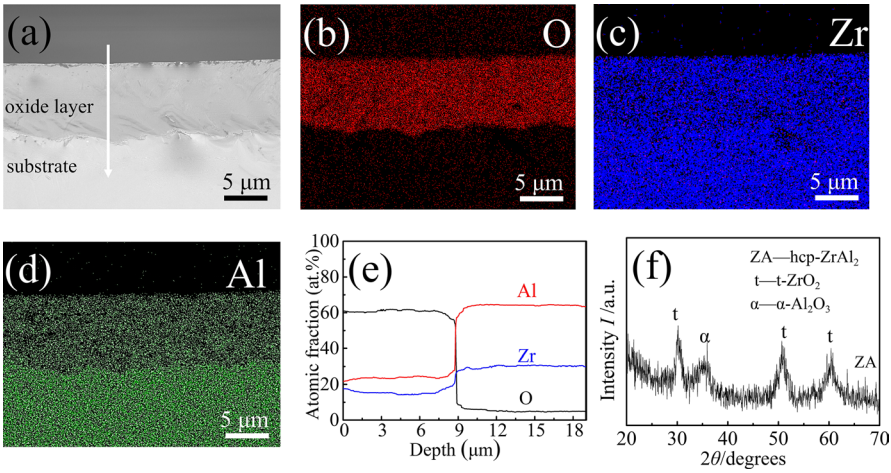

Fig. 5 **a** Cross-sectional BSE micrographs, image of **b** O, **c** Zr and **d** Al EDX mappings, **e** cross-sectional EDX line profile, and **f** XRD patterns of $ZrAl_2$ oxidized at 850 °C for 12 h. The white arrows in the figures indicate the scan direction of the EDX line

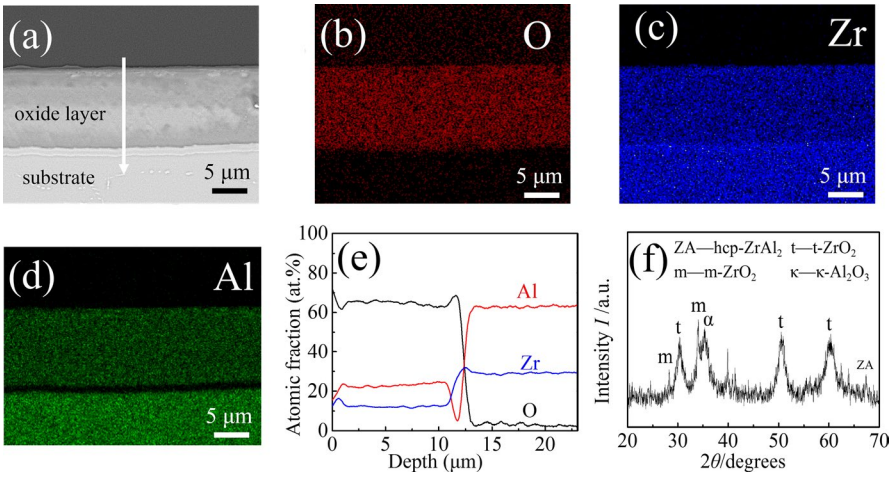

Fig. 6 **a** Cross-sectional BSE micrographs, image of **b** O, **c** Zr and **d** Al EDX mappings, **e** cross-sectional EDX line profile, and **f** XRD patterns of $ZrAl_2$ oxidized at 850 °C for 24 h. The white arrows in the figures indicate the scan direction of the EDX line

8 and 9. In addition to the peaks of hcp-$ZrAl_2$, diffraction peaks of tetragonal ZrO_2 (t-ZrO_2) and rhombohedral Al_2O_3 (α-Al_2O_3) were observed during the early oxidation stages (800 °C for 12 and 24 h and 850 °C for 12 h), as shown Figs. 3f, 4f and 5f. As oxidation continued, sharp diffraction peaks of monoclinic ZrO_2 (m-ZrO_2) and hexagonal Al_2O_3 (κ-Al_2O_3) emerged, in addition to those of the hcp-$ZrAl_2$, t-ZrO_2, and α-Al_2O_3 (Figs. 6, 7, 8, 9).

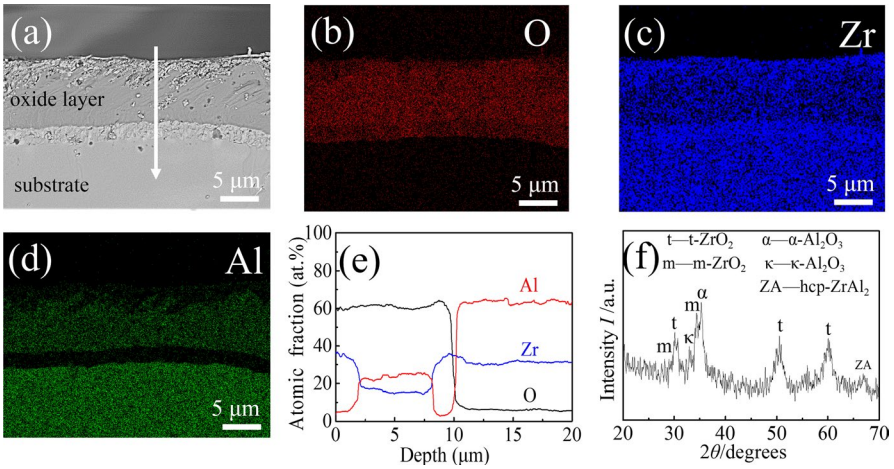

Fig. 7 **a** Cross-sectional BSE micrographs, image of **b** O, **c** Zr and **d** Al EDX mappings, **e** cross-sectional EDX line profile, and **f** XRD patterns of $ZrAl_2$ oxidized at 900 °C for 12 h. The white arrows in the figures indicate the scan direction of the EDX line

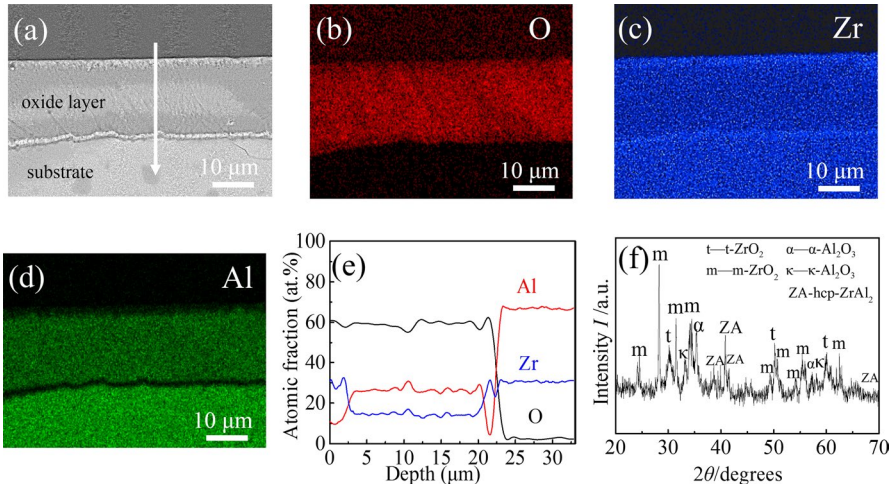

Fig. 8 **a** Cross-sectional BSE micrographs, image of **b** O, **c** Zr and **d** Al EDX mappings, **e** cross-sectional EDX line profile, and **f** XRD patterns of $ZrAl_2$ oxidized at 900 °C for 24 h. The white arrows in the figures indicate the scan direction of the EDX line

During the early stages of the oxidation of $ZrAl_2$, the cross-sectional BSE micrographs and elemental distribution mapping of the oxide layer indicated that a single-layer oxide was formed, e.g., as shown in Figs. 3 and 4 (800 °C, 12 and 24 h, respectively). According to the cross-sectional BSE micrographs, the oxide layer thicknesses after oxidation at 800 °C for 12 and 24 h were 6.8 ± 0.3 and 8.9 ± 0.2 μm, respectively. From the EDX results in Figs. 3 and 4, the value of the Al/Zr ratio was

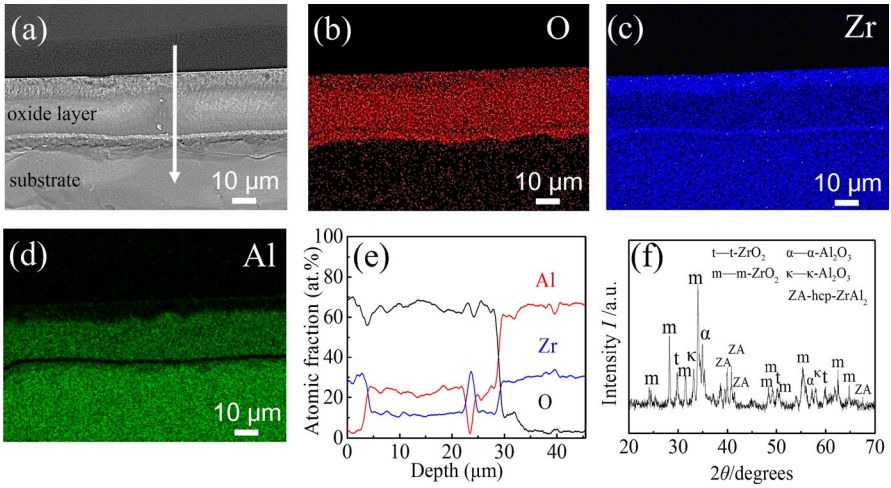

Fig. 9 **a** Cross-sectional BSE micrographs, image of **b** O, **c** Zr and **d** Al EDX mappings, **e** cross-sectional EDX line profile, and **f** XRD patterns of $ZrAl_2$ oxidized at 950 °C for 24 h. The white arrows in the figures indicate the scan direction of the EDX line

determined to be approximately two in the oxide layer and the $ZrAl_2$ substrate. Combined with the corresponding XRD pattern (Figs. 3, 4), it was concluded that the oxide layer was a single layer composed of a mixture of t-ZrO_2 and α-Al_2O_3.

After the oxidation of $ZrAl_2$ at higher temperatures and/or for longer oxidation times, the oxide layer evolved from a single layer to a multilayer structure (Figs. 6, 7, 8, 9). The cross-sectional BSE micrographs and the elemental distribution mapping of the oxide layer, as shown in Figs. 5 and 6 (850 °C, 12 and 24 h), show the evolution of the oxide layer from a single layer to a double-layer structure. The results of the cross-sectional BSE micrograph, EDX mapping, and line scan of the $ZrAl_2$ after oxidation at 850 °C for 12 h and the corresponding XRD pattern are shown in Fig. 5. These show that a single-layer oxide with a thickness of 8.5 ± 0.5 μm formed, and the value of the Al/Zr ratio was determined to be approximately two in the oxide layer. In combination with the corresponding XRD pattern, it follows that a single oxide layer composed of a uniform mixture of t-ZrO_2 and α-Al_2O_3 formed. The BSE micrograph and EDX analyses (mapping and line scanning) of the oxidized alloy (850 °C, 24 h), as presented in Fig. 6, show that a double-layer structure formed, with an outer layer thickness of 10.0 ± 0.1 μm and an inner layer thickness of 3.0 ± 0.1 μm. The value of the ratio of Al/Zr in the outer layer oxide was determined to be approximately two, and the inner oxide layer contained almost only Zr and O. Combined with the corresponding XRD pattern, it follows that the outer layer was composed of a mixture (t-ZrO_2 and α-Al_2O_3), and the inner layer was composed of only m-ZrO_2. Some of the Zr tended to diffuse outward to the surface of the oxide layer during the continued oxidation process, leading to slight Zr enrichment at the top surface (Figs. 6 and 7).

Figures 7, 8 and 9 show the cross-sectional BSE micrographs, the elemental mapping, and the XRD patterns of the $ZrAl_2$ alloy oxidized at 900 °C for 12 and 24 h

and at 950 °C for 24 h, respectively. The cross-sectional BSE micrographs show that oxide layers with multilayer structures formed at 900 °C (for 12 and 24 h) and at 950 °C (for 24 h). The results showed that the total oxide thicknesses formed at 900 °C for 12 and 24 h were 10.0 ± 0.2 μm (with an outermost layer thickness of ~ 2.3 μm, middle layer thickness of ~ 5.4 μm and innermost layer thickness of ~ 2.3 μm) and 22.0 ± 0.5 μm (with an outermost layer thickness of ~ 2.5 μm, middle layer thickness of ~ 17.5 μm and innermost layer thickness of ~ 2.0 μm), respectively. The EDX analyses of the three-layer oxide structure formed on $ZrAl_2$ after oxidation at 900 °C for 12 and 24 h both indicated that the Al concentrations were rather low in the outermost and innermost layers, and the Al/Zr ratio in the middle layer was about two (EDX mapping and line scans in Figs. 7 and 8, respectively). It follows that the outermost and innermost layers were composed of mainly ZrO_2, and the middle oxide was made up of a mixture (ZrO_2 and Al_2O_3). The corresponding XRD patterns shown in Figs. 7f and 8f indicate that the Al_2O_3 phase was mainly α-Al_2O_3, while the ZrO_2 phase transformed from t-ZrO_2 into m-ZrO_2 upon continued oxidation. The thickness of the oxide layer formed at 950 °C for 24 h was 29.0 ± 0.5 μm (with an outermost layer of ~ 4.8 μm, second layer of ~ 17.2 μm, third layer of ~ 2 μm and innermost layer of ~ 5 μm). The corresponding EDX analysis results, as shown in Fig. 9e, indicated that the Al concentrations were rather low in the outermost and third layers, and the Al/Zr ratios in the second and innermost layers were about two. Based on the EDX and XRD results (Fig. 9f), it was concluded that the outermost and third layer were composed of mainly m-ZrO_2, whereas the second and innermost layers were mainly composed of a mixture of m-ZrO_2 and α-Al_2O_3. No cracks or pores were generated in the entire oxide layer or the $ZrAl_2$ substrate during thermal oxidation of the alloy at different oxidation temperatures for different oxidation times.

Oxidation Kinetics

The mass gains during thermal oxidation of the alloy at different oxidation temperatures for different oxidation times are shown in Fig. 10a. To analyze the oxidation kinetics of the $ZrAl_2$ alloy, the relationship between the mass gain per unit area w and the oxidation time t were fitted using a parabolic rate equation (Eq. 1), and the Arrhenius relationship (Eq. 2) was used to determine the activation energy Q of the oxidation process [29]:

$$w(t)^2 = k(T)t, \tag{1}$$

$$k(T) = A \times \exp\left(-\frac{Q}{RT}\right), \tag{2}$$

where A, R, $k(T)$, and T are the pre-exponential factor, the gas constant, the temperature-dependent oxidation rate constant, and the absolute temperature, respectively. According to the fitting results shown in Fig. 10a, $ZrAl_2$ obeyed parabolic oxidation kinetics. $k(T)$ was determined to be 1.92×10^{-7}, 8.23×10^{-7}, 2.13×10^{-6},

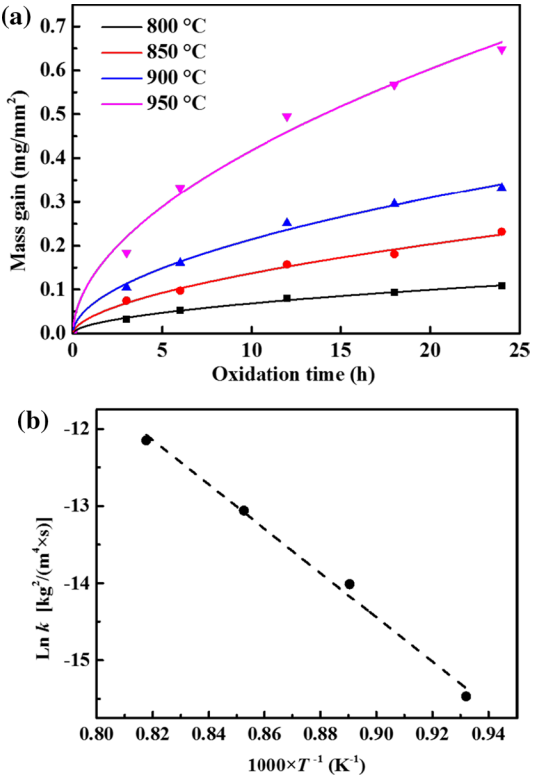

Fig. 10 **a** Measured mass gain of $ZrAl_2$ per unit surface area as a function of the oxidation time at 800, 850, 900 and 950 °C. **b** Arrhenius plot of the parabolic rate constant k for the oxidation of $ZrAl_2$ at 800, 850, 900 and 950 °C

and 5.30×10^{-6} kg^2/(m^4 s) at 800, 850, 900 and 950 °C, respectively. The Arrhenius plot and its fits are shown in Fig. 10b. The value of Q was thus determined to be 239 ± 14 kJ/mol.

Discussion

The parabolic oxidation kinetics in the oxidation temperature range of 800–950 °C indicate that the growth of the oxide layer was controlled by diffusion processes [30]. The newly formed ZrO_2 during the oxidation provided the main diffusion path for oxygen by forming oxygen vacancies, due to the non-metal deficient n-type structure of ZrO_2 [31, 32]. The activation energy for the oxidation is much higher at 800–950 °C (239 kJ/mol) than at 550–750 °C (143 kJ/mol) [28]. This is because of the formation of a dense multilayered oxide structure at higher oxidation temperatures, which effectively retarded the transport of oxygen [33]. An oxide layer without any pores and cracks was formed at the studied temperatures, because the addition of Zr in the alloy could improve the adhesion of the oxide layer on the alloy substrate [34–36].

The oxide layer transformed from a single-layer structure to a multilayer structure at 850 °C. This occurred because the alloy underwent uniform oxidation during the

early stages, and selective oxidation occurred during the later stages of oxidation. The $ZrAl_2$ alloy has undergone certain preferential oxidation of Zr at 850–950 °C, thus forming ZrO_2. According to the Al-Zr phase diagram shown in Fig. 1, a $ZrAl_3$ intermetallic phase might form as a result of the preferential oxidation of Zr. However, such preferential oxidation of Zr is much minor as compared to the simultaneous oxidation of Al and Zr (the thickness of ZrO_2 is much thinner than that of the mixed ZrO_2 and Al_2O_3 oxide layer; see Figs. 6, 7, 8, 9). As a result, the formation of, if any, $ZrAl_3$, could not be detected by SEM/EDX and XRD in the present work, and would only play a minor role in the oxidation mechanism. The mechanism for the transformation of the oxide layer structure from a single layer to a multilayer structure during oxidation can be explained as follows.

The single-layer oxide structure with a mixture of t-ZrO_2 and α-Al_2O_3 formed during the early oxidation stages is ascribed to the crystallization of the initially formed amorphous oxide. An amorphous oxide with a composition of $(Zr_{0.33}Al_{0.67})O_{1.66}$, as determined by EDX, formed at the alloy surface during heating at 800 °C for 3 h, similar to the case of the oxidation of the alloy in the 550–750 °C range [28]. Any long-range diffusion/redistribution of Al^{3+} and Zr^{4+} cations is difficult in amorphous oxides [37]. Thus, a uniform and single-layer oxide composed of crystalline Al_2O_3 and crystalline ZrO_2 formed during prolonged exposure.

The activities of Al and Zr in $ZrAl_2$ at 850 °C have been determined by CALPHAD method to be 2.1×10^{-2} and 3.4×10^{-4}, respectively. It is found that the activity of Al in $ZrAl_2$ is actually much higher than that of Zr, which would lead to a preferential oxidation of Al over Zr. In the present work, however, a preferential oxidation of Zr has been observed experimentally (Figs. 6, 7, 8, 9). The results thus indicate that such preferential oxidation of Zr is controlled thermodynamically by the lower Gibbs energy of formation of ZrO_2 as compared to Al_2O_3 (Fig. 11). Figure 11 shows the Gibbs energies of formation, $\Delta_f G^0$ (in kJ per mole O_2), at different temperatures (and at 1 atm) for various crystalline ZrO_2 and Al_2O_3 phases [38]. It follows that the two expected most stable oxide phases for the oxidation of the alloy at 800 °C were m-ZrO_2 and α-Al_2O_3, which is inconsistent with the XRD observations in this study (t-ZrO_2 and α-Al_2O_3). The formation of metastable t-ZrO_2, instead of m-ZrO_2, has previously been observed for the oxidation of Zr

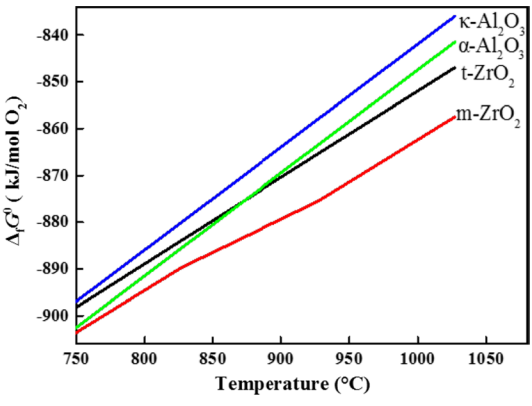

Fig. 11 Gibbs energies of formation, $\Delta_f G^0$ (kJ per mole O_2), at different temperatures (and 1 atm) for various pure crystalline ZrO_2 and Al_2O_3 phases [38]

alloys [39–41], which was mainly ascribed to the presence of domain boundaries and oxygen vacancies, which inhibited the transformation and stabilized the t-ZrO_2 phase [42, 43]. The oxidation process becomes much faster at higher temperatures. The corresponding large volume mismatch between the growing oxide and the original alloy substrate thus leads to a high internal stress in the oxide layer, which then drives the transformation of t-ZrO_2 to m-ZrO_2 at temperatures above 850 °C [44–48], as observed in Figs. 6, 7, 8 and 9.

It has been reported previously that the concentrations of Al and Zr in the reaction region that affect the oxidation reaction are key factors in the oxidation process [37, 49–51]. The $\Delta_f G^0$ value of Zr oxidization to form m-ZrO_2 was lower than that of Al oxidization to form Al_2O_3 at 850 °C, as demonstrated in Fig. 11. Therefore, Zr reacted more easily with oxygen than Al did above 850 °C, and as a result, the Zr located under the mixed oxide layer formed an m-ZrO_2 layer upon oxidation. During the later oxidation stages, ZrO_2 was more likely to form than Al_2O_3 on the $ZrAl_2$ surface. Once a ZrO_2 layer formed, oxygen continuously diffused into the $ZrAl_2$ substrate through the ZrO_2 layer. The consumption of Zr (to form ZrO_2) at the outermost surface of $ZrAl_2$ alloy could lead to the formation of a region of Al enrichment and thus increase the activity of Al [52] beneath the ZrO_2 layer. Thus, the Al and Zr could react simultaneously to form a mixed Al_2O_3 and ZrO_2 oxide layer beneath the ZrO_2 layer. The influence of the high oxygen activity of Al gradually decreased due to the consumption of Al upon the thickening of the mixed Al_2O_3–ZrO_2 oxide layer. Thus, the effect of the high oxygen affinity of Zr dominated again beneath the mixed oxide layer, leading to the formation of a second ZrO_2 oxide layer. With the consumption of the Zr to form ZrO_2, Al and Zr were simultaneously oxidized to form a mixed layer of Al_2O_3 and ZrO_2 in the Al-rich region beneath the ZrO_2 layer again. Thus, the oxide layer was composed of alternating layers of ZrO_2 and a mixture of ZrO_2 and Al_2O_3 during the later stages of oxidation due to the competing influences of the slightly higher affinity of oxygen for Zr than for Al and the enrichment/redistribution of the reacting elements induced by oxidation in front of the oxidation-reaction region.

Conclusion

The thermal oxidation of $ZrAl_2$ in pure O_2 at 800–950 °C was studied comprehensively. The $ZrAl_2$ followed parabolic oxidation kinetics with an activation energy of 239 ± 14 kJ/mol. A single-layer oxide structure composed of a mixture of ZrO_2 and Al_2O_3 formed below 850 °C, which transformed into a multilayer oxide structure containing alternating layers of ZrO_2 and a ZrO_2–Al_2O_3 mixture at higher temperatures. The mechanism for the transformation of the oxide layer structure from a single layer to a multilayer structure is as follows: i) the crystallization of the initially formed amorphous oxide layer resulted in uniform oxidation during the early stages of oxidation; ii) the structure of the oxide layer transformed into a multilayer structure during the later stages of oxidation due to the competitive effect of the high Zr affinity for oxygen and the concentration instability in the sublayer region. Since Al and Zr have very similarly high affinities toward oxygen, the findings are helpful to

understand the oxidation behavior of multi-component alloys which often contain several elements with similarly oxygen affinities.

Acknowledgements The authors are grateful to Dr. Hong Bo (Yanshan University, China) for help with CALPHAD calculations. This work was supported by the National Natural Science Foundation of China (No. 51571148) and the National Key Research and Development Program of China (Nos. 2017YFE0302600 and 2017YFB0701801).

References

1. H.H. Kung, Transition metal oxides: surface chemistry and catalysis, Elsevier, 1989.
2. V. Fiorentini, G. Gulleri, Theoretical evaluation of zirconia and hafnia as gate oxides for Si microelectronics, Physical review letters, **89**, 266101 (2002).
3. Y. Wang, X. Wang, K. Wu, F. Wang, Role of Al18B4O33 Whisker in MAO Process of Mg Matrix Composite and Protective Properties of the Oxidation Coating, Journal of Materials Science & Technology, **29**, 267 (2013).
4. D. Kim, S.-L. Shang, Z. Li, B. Gleeson, Z.-K. Liu, Effects of Hf, Y, and Zr on Alumina Scale Growth on NiAlCr and NiAlPt Alloys, Oxidation of Metals, **92**, 303 (2019).
5. K. Weller, Z.M. Wang, L.P.H. Jeurgens, E.J. Mittemeijer, Oxidation kinetics of amorphous AlxZr1 − x alloys, Acta Materialia, **103**, 311 (2016).
6. Y. Xu, L.P.H. Jeurgens, Y. Huang, et al., Effect of structural order on oxidation kinetics and oxide phase evolution of Al–Zr alloys, Corrosion Science, **165**, 108407 (2020).
7. E.F. Ibrahim, B.A. Cheadle, Development of Zirconium Alloys for Pressure Tubes in Candu Reactors, Canadian Metallurgical Quarterly, **24**, 273 (1985).
8. J. Yang, A. Sudik, C. Wolverton, D.J. Siegel, High capacity hydrogen storage materials: attributes for automotive applications and techniques for materials discovery, Chemical Society Reviews, **39**, 656 (2010).
9. N. Ni, S. Lozano-Perez, M.L. Jenkins, et al., Porosity in oxides on zirconium fuel cladding alloys, and its importance in controlling oxidation rates, Scripta Materialia, **62**, 564 (2010).
10. T.-S. Jung, H. Jang, Y.-K. Mok, J.-S. Yoo, Analysis of EBSD image quality related to microstructure evolution in zirconium–niobium cladding to quantify the degree of recrystallization, Journal of Nuclear Materials, **509**, 188 (2018).
11. Y. Ding, J.-S. Kim, H. Kim, et al., Evaluation of anisotropic deformation behaviors in H-charged Zircaloy-4 tube, Journal of Nuclear Materials, **508**, 440 (2018).
12. T. Wang, Z. Jin, J.C. Zhao, Thermodynamic assessment of the Al-Zr binary system, Journal of Phase Equilibria, **22**, 544 (2001).
13. M. Alatalo, M. Weinert, R.E. Watson, Stability of Zr-Al alloys, Physical Review B, **57**, R2009 (1998).
14. T. Wei, X. Dai, B. Chen, J. Zhang, C. Long, Nodular Corrosion of Zr–0.85Sn–0.16Nb–0.37Fe–0.18Cr Alloy in 500 °C Steam Caused by High-temperature Processing, Oxidation of Metals, **92**, 493 (2019).
15. Z. Zhu, J. Shi, C. Yao, et al., Positron Annihilation Study of High-Temperature Oxidation Behavior of Zr–1Nb Alloy, Oxidation of Metals, **90**, 657 (2018).
16. B. Cox, Hydrogen uptake during oxidation of zirconium alloys, Journal of Alloys and Compounds, **256**, 244 (1997).
17. J. Sun, J. Liu, L. Liu, et al., Effects of Al on microstructural stability and related stress-rupture properties of a third-generation single crystal superalloy, Journal of Materials Science & Technology, **35**, 2537 (2019).
18. X.J. Jiang, Y.Y. Zhang, C.L. Li, et al., Microstructure and mechanical properties of ZrAl binary alloys, Journal of Alloys and Compounds, **811**, 152068 (2019).
19. M. Negyesi, M. Amaya, The Effect of Air Fraction in Steam on the Embrittlement of Zry-4 Fuel Cladding Oxidized at 1273–1573 K, Oxidation of Metals, **92**, 439 (2019).
20. V. Babic, C. Geers, I. Panas, Reactive Element Effects in High-Temperature Alloys Disentangled, Oxidation of Metals, (2019).

21. H.Y. Kim, K. Nakai, J. Fu, S. Miyazaki, Effect of Al addition on superelastic properties of Ti–Zr–Nb-based alloys, Functional Materials Letters, **10**, 1740002 (2017).
22. A.H. Cai, J. Tan, D.W. Ding, H. Wang, G.J. Zhou, Effect of Al addition on properties of Cu45Zr45.5Ti9.5 bulk metallic glass, Materials Chemistry and Physics, **251**, 123072 (2020).
23. J. Du, B. Wen, R. Melnik, Y. Kawazoe, Cluster characteristics and physical properties of binary Al–Zr intermetallic compounds from first principles studies, Computational Materials Science, **103**,170 (2015).
24. Y.H. Duan, B. Huang, Y. Sun, M.J. Peng, S.G. Zhou, Stability, elastic properties and electronic structures of the stable Zr–Al intermetallic compounds: A first-principles investigation, Journal of Alloys and Compounds, **590**, 50 (2014).
25. J. Murray, A. Peruzzi, J.P. Abriata, The Al-Zr (aluminum-zirconium) system, Journal of Phase Equilibria, **13,** 277 (1992).
26. W.-C. Hu, Y. Liu, D.-J. Li, X.-Q. Zeng, C.-S. Xu, First-principles study of structural and electronic properties of C14-type Laves phase Al2Zr and Al2Hf, Computational Materials Science, **83**, 27 (2014).
27. X. Tao, Y. Ouyang, H. Liu, et al., Ab initio calculation of the total energy and elastic properties of Laves phase C15 Al2RE (RE = Sc, Y, La, Ce–Lu), Computational Materials Science, **44**, 392 (2008).
28. Z. Hu, Y. Xu, Y. Chen, et al., Anomalous formation of micrometer-thick amorphous oxide surficial layers during high-temperature oxidation of ZrAl2, Journal of Materials Science & Technology, **35**, 1479 (2019).
29. P. Kofstad, High temperature corrosion, Elsevier Applied Science Publishers, Crown House, Linton Road, Barking, Essex IG 11 8 JU, UK, 1988., (1988).
30. N. Birks, G.H. Meier, F.S. Pettit, Introduction to the high temperature oxidation of metals, Cambridge University Press, 2006.
31. D.B. Lee, S.W. Woo, High temperature oxidation of Ti–47%Al–1.7%W–3.7%Zr alloys, Intermetallics, **13**, 169 (2005).
32. S.J. Qu, S.Q. Tang, A.H. Feng, et al., Microstructural evolution and high-temperature oxidation mechanisms of a titanium aluminide based alloy, Acta Materialia, **148**, 300 (2018).
33. D.B. Lee, M.L. Santella, High temperature oxidation of Ni3Al alloy containing Cr, Zr, Mo, and B, Materials Science and Engineering: A, **374**, 217 (2004).
34. C.T. Sims, N.S. Stoloff, W.C. Hagel, superalloys II, Wiley New York, 1987.
35. S. Chevalier, P. Juzon, G. Borchardt, et al., High-Temperature Oxidation of Fe3Al and Fe3Al–Zr Intermetallics, Oxidation of Metals, **73**, 43 (2010).
36. A. Hotař, P. Kejzlar, M. Palm, J. Mlnařík, The effect of Zr on high-temperature oxidation behaviour of Fe3Al-based alloys, Corrosion Science, **100**, 147 (2015).
37. X. Sun, S. Schneider, U. Geyer, W. Johnson, M.A. Nicolet, Oxidation and crystallization of an amorphous Zr60Al15Ni25 alloy, 1996.
38. P.J. Linstrom, W.G. Mallard, The NIST Chemistry WebBook: A Chemical Data Resource on the Internet, Journal of Chemical & Engineering Data, **46**, 1059 (2001).
39. W. Kai, H.H. Hsieh, Y.R. Chen, Y.F. Wang, C. Dong, Oxidation behavior of an Zr53Ni23.5Al23.5 bulk metallic glass at 400–600°C, Intermetallics, **15**, 1459 (2007).
40. T. Chraska, A.H. King, C.C. Berndt, On the size-dependent phase transformation in nanoparticulate zirconia, Materials Science and Engineering: A, **286**, 169 (2000).
41. Y. Xu, X. Liu, L. Gu, et al., Natural oxidation of amorphous CuxZr1-x alloys, Applied Surface Science, **457**, 396 (2018).
42. T. Mitsuhashi, M. Ichihara, U. Tatsuke, Characterization and Stabilization of Metastable Tetragonal ZrO2, Journal of the American Ceramic Society, **57**, 97 (1974).
43. R. Srinivasan, L. Rice, B. Davis, Critical Particle Size and Phase Transformation in Zirconia: Transmission Electron Microscopy and X-Ray Diffraction Studies, 2005.
44. D. Huang, L. Huang, B. Wang, V. Ji, T. Zhang, The relationship between t-ZrO2 stability and the crystallization of a Zr-based bulk metallic glass during oxidation, Intermetallics, **31**, 21 (2012).
45. T.K. Gupta, F.F. Lange, J.H. Bechtold, Effect of stress-induced phase transformation on the properties of polycrystalline zirconia containing metastable tetragonal phase, Journal of Materials Science, **13**, 1464 (1978).
46. O. Bernard, A.M. Huntz, M. Andrieux, et al., Synthesis, structure, microstructure and mechanical characteristics of MOCVD deposited zirconia films, Applied Surface Science, **253**, 4626 (2007).

47. X.-S. Zhao, S.-L. Shang, Z.-K. Liu, J.-Y. Shen, Elastic properties of cubic, tetragonal and monoclinic ZrO2 from first-principles calculations, Journal of Nuclear Materials, **415**, 13 (2011).
48. D.L. Beke, I.A. Szabó, Z. Erdélyi, G. Opposits, Diffusion-induced stresses and their relaxation, Materials Science and Engineering: A, **387-389**, 4 (2004).
49. W. Hemminger, Thermochemical data of pure substances, parts I and II: I. Barin, published by VCH, Weinheim, Germany, ISBN 3-527-27812-5, 1739 pages; DM 680, Thermochimica Acta, **222**, 305 (1993).
50. H.Q. Ye, Recent developments in Ti3Al and TiAl intermetallics research in China, Materials Science and Engineering: A, **263**, 289 (1999).
51. D. Wei, J. Li, T. Zhang, H. Kou, High-Temperature Oxidation Behavior of Ti-22Al-27(Nb, Zr) Alloys, Rare Metal Materials & Engineering, **44**, 261 (2015).
52. D.B. Lee, S.W. Woo, High temperature oxidation of Ti–47% Al–1.7% W–3.7% Zr alloys, Intermetallics, **13**, 169 (2005).